Chapter 5

Evolution of nanocluster size distribution in nanocluster aggregation source

The results obtained with our setup for producing nanoclusters (see Chapter 2) are presented. First we study the influence of experimental conditions on the morphology and density of nanoparticles deposited on a substrate outside the aggregation chamber. Then, using this information, we focus on the processes governing formation of Cu nanoparticles inside the aggregation chamber. The evolution of morphology and the particle size distribution at different pressure and type of inert gas (Ar and Kr) is investigated with TEM. The experimental data are compared to simulation results obtained with the model of cluster formation and coagulation in the inert gas which has been formulated in Chapter 4. It is shown that model predictions agree well with experimental data.

5.1 Introduction

The increasing interest in the production of nanoclusters and nanoparticles of a certain size is driven by the remarkable variations in electrical, optical and magnetic properties that occur as one down size from a bulk to a particle of material consisting of a countable number of atoms [1]. Size-dependent characteristics open a possibility for tuning properties of nanoclusters by precisely controlling the formation process [2]. From a technological point of view, nanoclusters can be considered as a component for a new generation of nanostructured devices and materials. However, producing such materials, presents its own challenges related to understanding the physical and chemical mechanisms that govern their assembly and properties [3].

There exist various methods for synthesis of nanoclusters (see Chapter 2). In Chapter 5 we consider nanoclusters production by a gas aggregation technique [4], where hot atoms, generated by the vaporization of the target material, are cooled and

condensed in a cold inert buffer gas to create the clusters. Plasma sputtering with a magnetron ion source provides a method of vaporizing a wide range of materials [5]. Clusters grow in the aggregation chamber until the mixture of gas and clusters is released through an aperture into a surrounding vacuum chamber. By changing the experimental conditions the particle morphology and the particle size distribution can be controlled to produce nanoparticles with optimal properties.

Here, we study formation of Cu nanoclusters in the experimental setup based on a NC200-UHV nanocluster source, which is described in Chapter 2. First, a series of experiments was carried out to explore the capabilities of the setup. Then more detailed experiments were performed to study kinetics of cluster formation *inside the aggregation chamber* with two types of gas, Ar and Kr, and at two different pressures, 20 and 40 Pa. The morphology and the size distribution of produced nanoclusters were characterized with TEM and image analysis technique described in Chapter 3. The experimental data is compared to simulation results obtained with the kinetic model developed in [6] and described in Chapter 4.

5.2 Experimental study of nanoparticles formation at different conditions

5.2.1 Experimental setup: control parameters and capabilities

The experimental setup has been built in our laboratory using NC200-UHV cluster source and other components. As described in Chapter 2, a number of parameters of the cluster source NC200-UHV can be varied. This leads to different size and shape of the clusters. The following parameters have significant influence: aggregation length, gas flow rate, aperture size, magnetron power, material of target [7]. It is important to note that change of a single parameter sometimes have quite complex effects and may depend on the other settings. An example of such effect is alteration of gas flow rate or type of the gas; it changes the sputter yield from the target. Therefore it is necessary to control the influence of every parameter changed and take it into account during data analysis. For this reason, several basic tests need to be done to understand capabilities of the setup and to be able to plan further experiments. We started this study by checking two parameters that can be varied, while keeping the other parameters constant: the deposition time and aggregation length.

The first experiments were done to find the deposition time required to produce the concentration of particles on the substrate in deposition chamber, which is suitable for further analysis. The initial duration of experiment was 60 seconds. As

can be seen on Fig. 5.1, the concentration of particles is too high. Such images are not suitable for nanoparticle characterization because of nanoparticle overlapping. The results of experiments with the reduced deposition time (20 and 10 seconds) are presented in Fig. 5.1. The former one still has too many particles, so the duration of 10 s was chosen in further experiments.

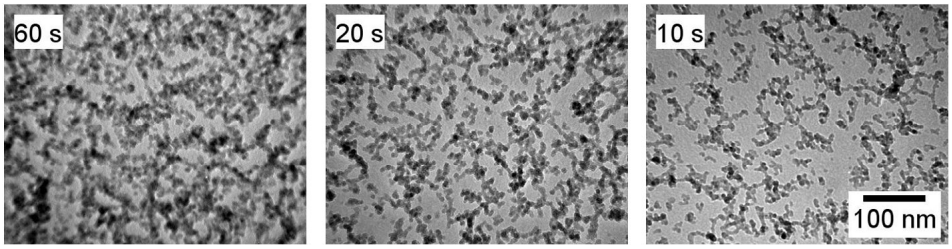

Figure 5.1. TEM micrographs showing dependence of clusters concentration on deposition time.

As can be seen from Fig. 5.1 deposited particles are agglomerates of smaller particles, i.e. they exhibit dendritic or fractal-like structure. When analyzing such images, important question arises, whether the agglomerate we see was deposited as is or they were formed on the substrate from spherical particles due to surface diffusion. To verify this, we performed experiment with deposition time of 1 s. Such short time significantly reduces overlapping on the substrate (Fig. 5.2). However, the morphology of particles remains fractal-like. This experiment shows that agglomerates are formed in the aggregation chamber.

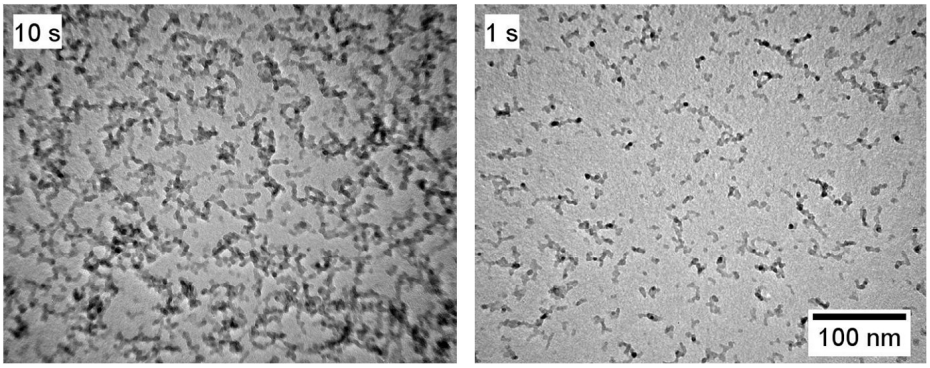

Figure 5.2. Samples produced with a deposition time of 10 and 1s. Fractal-like morphology present in both cases, suggesting the agglomerates formed in the aggregation chamber.

The aggregation length is defined as a distance between the magnetron and the aperture. It can be adjusted by means of a linear motion drive from 50 to 200 mm.

This allows one to vary the residence time of particles, and hence their size and shape. To study this dependence we made a series of experiments with different aggregation lengths. The results showed significant change in concentration, while size of primary particles remains the same (Fig. 5.3). Discussion of this dependence is presented later in this chapter.

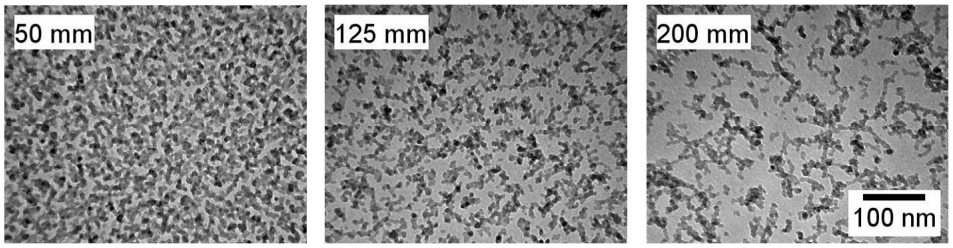

Figure 5.3. TEM images of Cu agglomerates obtained using different aggregation lengths.

Another parameter that influences the residence time of particles in the aggregation chamber is the aperture size. At smaller aperture diameter the drift velocity of the buffer gas decreases, leading to a longer residence time and consequently larger clusters and agglomerates. Samples produced with two different aperture diameters of 1 and 3 mm are shown in Fig. 5.4. From these images it is clear that the aperture size has a substantial influence on the formation of nanoclusters. In this example the mean diameter of clusters was increased 5 times: from about 4 nm using 3 mm aperture, to about 20 nm for 1 mm aperture.

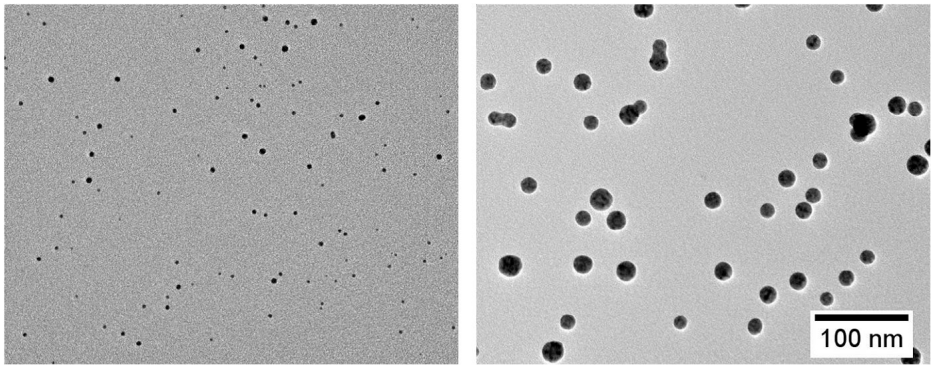

Figure 5.4. Influence of aperture size on the formation of Ag nanoclusters. Samples obtained with aperture diameter of 3 mm (left) and 1 mm (right).

Pressure in the aggregation chamber is determined by both the aperture size and the gas flow rate. As mentioned earlier, the gas flow rate influences also the sputter yield form the target. For this reason, it is not possible to compare directly

the results obtained at different pressures (Fig. 5.5). First it is necessary to process the data and then use a suitable model to account for the effect of pressure.

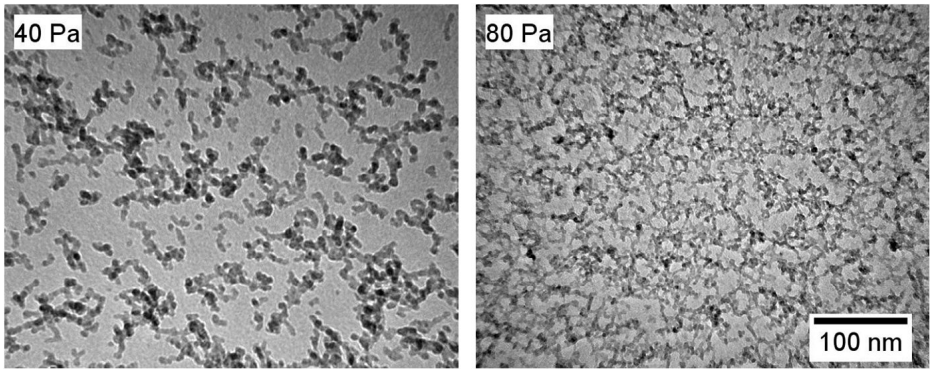

Figure 5.5. Influence of pressure in the aggregation chamber on the morphology of deposited Cu particles.

The performed experiments and results achieved give us essential information and fundamental understanding of the cluster source capabilities. They also show the influence and importance of the deposition parameters. As we have seen, agglomerate formation takes place already in the aggregation chamber. In order to better understand the kinetics of cluster formation, we will focus our examination on processes inside the aggregation chamber.

5.2.2 Cluster formation in aggregation chamber

As mentioned before in our experiments metal atoms are sputtered from a pure copper target and condensed into clusters within an inert gas filled aggregation chamber. Due to a high flux of Cu from the magnetron sputtering device, a suitable deposition time for all the samples was 15 seconds. Experiments were performed with two types of gas, Ar and Kr, and at two different pressures, 20 and 40 Pa (Table 5.1). For a comparison among samples obtained at different conditions, it is essential to know the sputtering yield which was evaluated by measuring the mass loss of the target after hour-long deposition for each experimental condition.

The choice of the specific gas was made according to the elastic-collision theory [8] which suggests that for an efficient momentum transfer, the atomic weight of the sputtering gas should be close to the atomic weight of the target. Note that the gas pressure change leads to changes in copper yield from the target (Table 5.1).

The clusters were deposited onto a 20 nm thick amorphous carbon film, supported by Cu grid for analysis in a JEOL 2010F transmission electron microscope (TEM) operated at 200 kV. TEM images of each sample have been

taken at two magnifications. The lower magnification images (x100k) were used to evaluate the surface density of Cu nanoparticles, whereas the morphology of the nanoparticles was determined from the higher magnification images (x300k). This approach helped to characterize nanoparticles with a high accuracy by either large number of objects or high resolution images when necessary. A sufficient number of images was acquired to allow the evaluation of more than 100 individual aggregates per sample.

Table 5.1. Experimental conditions for nanocluster formation.

Type of buffer gas	*Pressure,* P_g*, Pa*	*Gas flow rate, sccm*	*Copper yield,* Q_{Cu}*, mgr/hr*
Argon	20	8.4	358
Argon	40	16.8	270
Krypton	20	8.4	310
Krypton	40	16.8	186

Image pre-processing and analysis were performed using a MATLAB software package following closely the procedures described in the literature [9-11] Aggregates that touch edges of images were excluded from the analysis, as there were aggregates having too low contrast to the background. Using a custom written MATLAB code (section 3.4) the images were analyzed to determine the projected area of agglomerate, its maximum projected length L and width W in the direction perpendicular to L.

First, in order to check predictions of the model (Chapter 4) concerning diffusion of clusters in the aggregation chamber we have performed an experiment. A stripe of stainless steel was placed inside the aggregation chamber along the cylindrical wall. After several minutes the sputtered copper deposited to the stripe (Fig. 5.6). The color of the stripe changes along it demonstrating the dependence of cluster deposition rate onto the walls on cluster size.

The part of the stripe which was close to the magnetron exhibited a typical red color of polished copper indicating that copper atoms and small clusters deposited onto this part. The mid-portion of the stripe was black because of cluster deposition. The part of stripe near the aperture did not change its color. i.e. a very small number of clusters deposited here. We interpret this as a consequence of slow diffusion of large clusters in radial direction, i.e. in the aggregation chamber with the flow of buffer gas the small-sized clusters are effectively removed from the cluster population. Therefore to visualize the deposited particles and check our

assumptions, the same experiment was repeated with TEM grids placed at distinct positions on the top of the stripe. The results are shown in Fig. 5.7.

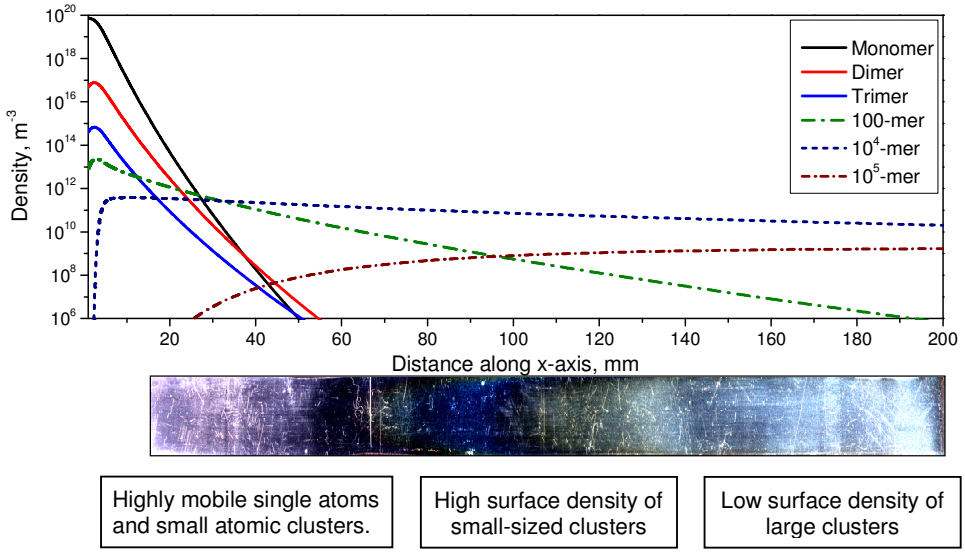

Figure 5.6. Diffusion-controlled deposition of copper atoms and nanoclusters onto the stripe of stainless steel placed inside the aggregation chamber along the cylindrical wall. The argon pressure 40 Pa, other parameters are listed in Tables 5.1 and 5.2. The plot shows the dependence of cluster densities along the aggregation tube obtained with the model of Chapter 4.

To study the cluster formation process we examine the samples obtained at 4 different conditions mentioned earlier. To evaluate the size distribution as a function of distance from the target, the TEM grids were placed inside the aggregation tube, close to its axis at distances of 50, 80, 120 and 170 mm from the target. For all the experimental conditions at a distance of 50 mm the deposition rate was very high, resulting in a film with densely packed nanoclusters (Fig. 5.8a). Therefore, such samples were not possible to analyze using image processing algorithms.

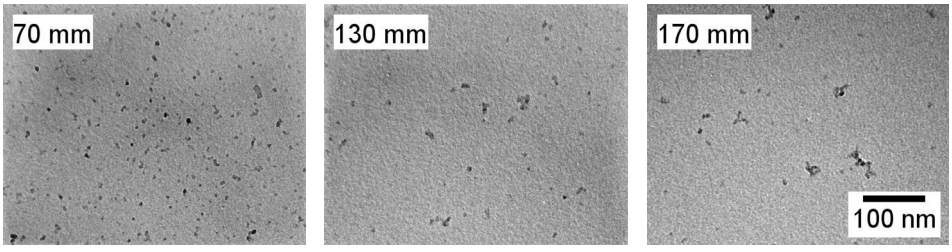

Figure 5.7. Nanoparticles deposited on TEM grids positioned on the strip at different distances from the magnetron within the aggregation chamber.

Further downstream, at the distance of 80 mm, well defined separate clusters were formed. Although, at certain conditions, many small clusters (less than 2 nm), almost indistinguishable from the background, were also seen on the substrate (Fig. 5.8b). The presence of these small clusters was confirmed by high-resolution TEM images and energy-dispersive X-ray spectroscopy (EDS). For this reason, all the samples collected at distances of 50 and 80 mm were rejected for the further image analysis as well as for the comparison with model calculations.

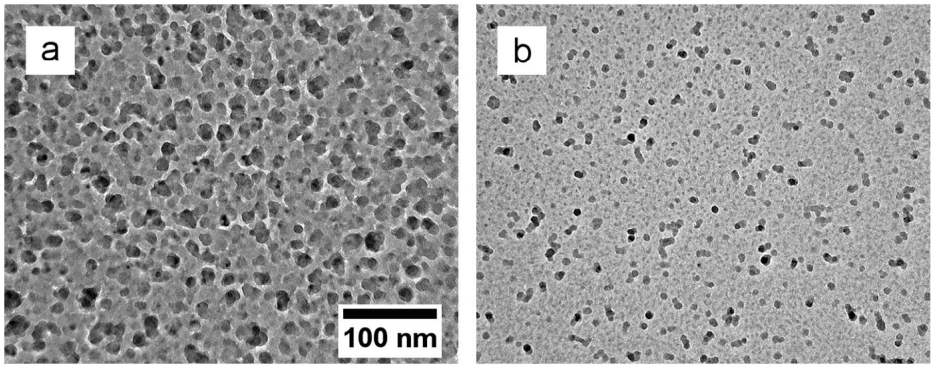

Figure 5.8. An example of samples not suitable for image processing: (a) film of clusters formed at the distance of 50mm from the target and (b) well defined clusters with many small particles between them (collected at 80mm). Such samples were rejected from further analysis.

TEM images of collected nanoparticles are presented in Fig. 5.9. As can be seen for both samples using Ar gas, at 120 mm the deposited particles have a compact shape close to spherical one with the mean diameter about 8 nm. Whereas at 170 mm, nanoparticles formed at the pressure of 20 Pa still have compact shape, the ones formed at 40 Pa are undoubtedly dendrite-like with maximum sizes in the range of 50 nm. The other noticeable difference between these two samples is the surface density, which is much higher for 20 Pa at 120 mm, but lower at 170 mm. The particles formed using Kr gas are larger comparing to the ones formed with Ar gas, their mean diameter is about 12 nm. However, the morphology did not change significantly, only the surface density becomes lower downstream.

Fig. 5.9 (lower row) shows the TEM images of samples collected after the aperture. At the same experimental conditions there is a significant difference between populations of nanoparticles collected 30 mm before the aperture and after it. This effect is caused by the flow of buffer gas with suspended nanoparticles through the aperture. However, aggregates of nanoparticles collected after the aperture consist of primary particles of about the same diameter as the nanoparticles before the aperture. Additional experiments with shorter deposition times or lower

deposition rates, to avoid overlapping of particles on the substrate, might clarify this observation. However this question lies outside of the scope of this work.

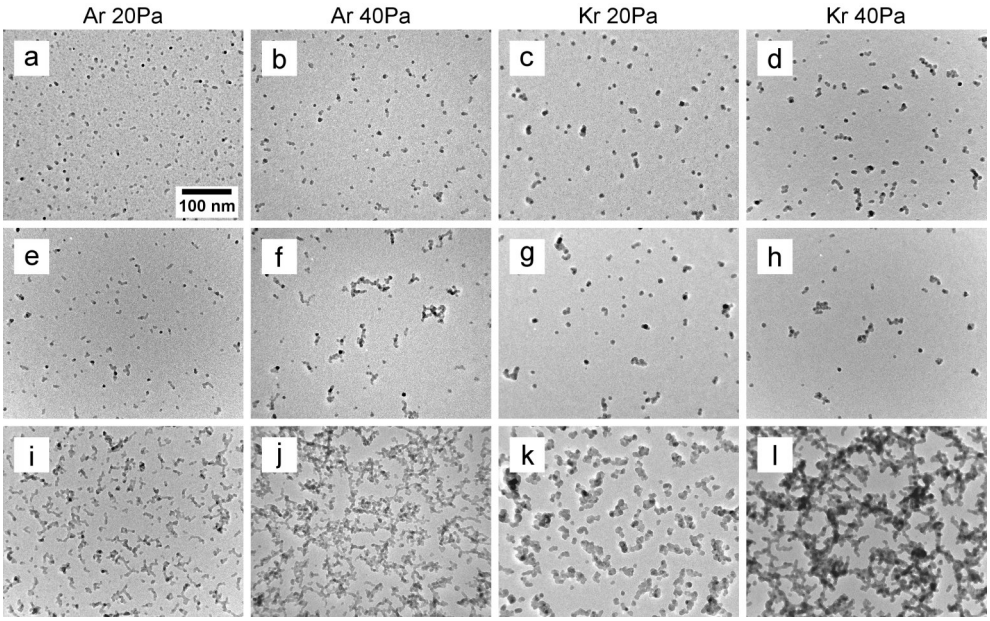

Figure 5.9. TEM images of Cu clusters collected inside the aggregation tube close to its axis during deposition time 15 s at the distance of 120mm (a-d), 170 (e-f) from the target, and after the aperture (i-l). Scale bar is the same for all images.

5.3 Comparison of experimental and model results

The area density of deposited cluster N_S was measured experimentally from 3 TEM images, containing in total at least 80 objects. The total volume density of clusters $N_V = \sum_{k>1} C_k$ was derived from N_S using the relation

$$N_S = N_V v t \ , \tag{5.1}$$

where v is the gas flow velocity (4.26), t = 15 s is the deposition time.

The nanocluster PSD $F_V^{\exp}(n)$ was reconstructed from the surface distribution $F_S(A)$ over the cluster projected area A. The surface distributions of nanoclusters deposited to amorphous carbon substrates inside the aggregation tube were derived from analysis of TEM images (average of 3 images). To relate the aggregate projected area A with the number of atoms n in it we used the corresponding formula from reference [12]

$$n = k_0 k_a \left(\frac{A}{\pi r_{Cu}^2 k_0^{2/3}} \right)^{\alpha_a}, \tag{5.2}$$

where k_a and α_a were treated as the fitting parameters when comparing simulation results with experimental PSD. The reconstructed PSD $F_V^{\exp}(n)$ is given by

$$F_V^{\exp}(n) = \frac{F_S(A)}{vt} \frac{dA}{dn}. \tag{5.3}$$

The coagulation equations (4.40)-(4.43) were solved numerically by the method described in section 4.4 using parameters listed in Tables 5.1 and 5.2. The parameters k_0, D_f^∞ and sticking coefficients η_{12}, η_{13} and η_{22} were adjusted to obtain a good agreement with measured volume density and PSD. It is noteworthy that D_f^∞ = 1.8 is close to the value observed during diffusion limited cluster aggregation [12-14].

Table 5.2. Parameters used for simulation of nanocluster formation.

Parameter	*Value*
Length of aggregation chamber, L, mm	200
Radius of aggregation chamber, R,mm	50
Aperture diameter, a, mm	3
Temperature, T, K	300
Sticking coefficient for the dimer formation in Ar, η_{11}	$1.8\times10^3 C_{Ar} r_{Ar}^3$
Sticking coefficient for the dimer formation in Kr, η_{11}	$1.28\times10^3 C_{Kr} r_{Kr}^3$
Fractal dimension of large clusters, D_f^∞	1.8
Maximum number of atoms in a cluster with $D_f(k) = 3$, k_0	1100
Parameter k_a, equation (5.2)	1.1
Parameter α_a, equation (5.2)	1.6

Comparison between experimental and model distributions is presented in Figs. 5.10 and 5.11. Figure 5.10 shows that the increase in Ar pressure enhances the coagulation, i.e. the distribution becomes broader. The reason is that according to (4.27) the cluster diffusivity decreases. Hence, the cluster losses to the wall reduce.

In case of Kr buffer gas this effect is not observed (Fig. 5.11), probably because with increase of the Kr pressure the copper yield decreases substantially (Table 5.1). Note that model distributions were calculated with the same set of parameters both for Ar and Kr, except for the sticking coefficients η_{12}, η_{13} and η_{22} indicated in figure captions. Calculation of sticking coefficients lies outside of the scope of this work, since it requires detailed knowledge of interaction between gas atoms and clusters at the atomic level.

In Fig. 5.12 the dependence of nanoparticle volume density on the distance along the aggregation tube is compared with the volume density predicted by the model for experimental conditions studied.

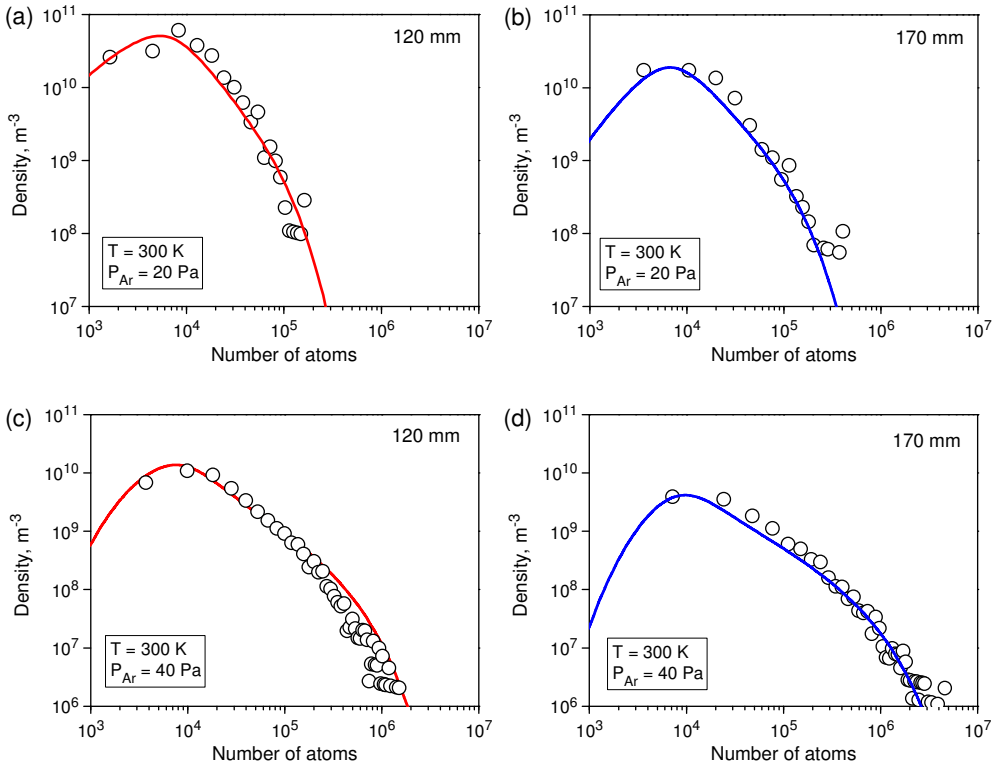

Figure 5.10. The size distribution of nanoclusters at distances 120 and 170 mm from the Cu target. Argon was used as the buffer gas. (a) and (b) argon pressure 20 Pa. (c) and (d) argon pressure 40 Pa. Symbols correspond to experimental distributions $F_V^{\exp}(n)$ *reconstructed from surface distributions* $F_S(A)$ *using (5.2) and (5.3). The solid line shows results of modeling. Sticking coefficients* $\eta_{12} = 2x10^2\,\eta_{11}$ *and* $\eta_{13} = \eta_{22} = 10^4\,\eta_{11}$.

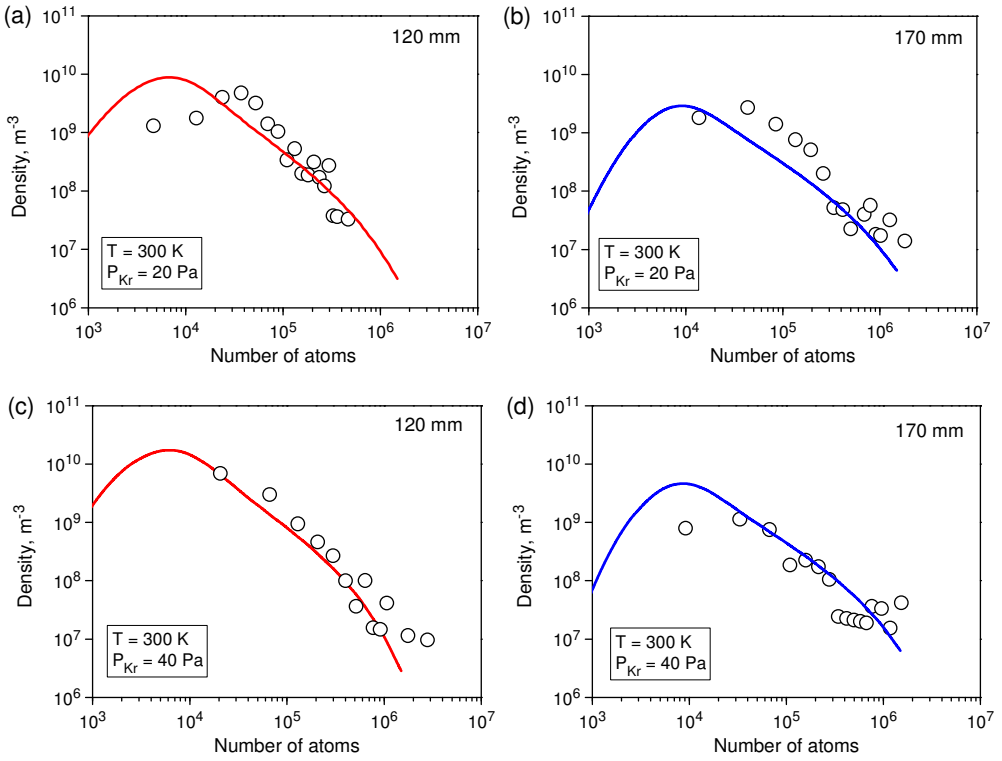

Figure 5.11. The size distribution of nanoclusters in the aggregation tube filled with krypton. (a) and (b) krypton pressure 20 Pa. (c) and (d) krypton pressure 40 Pa. Distances from the Cu target are indicated in figures. Symbols correspond to experimental distributions $F_V^{\exp}(n)$. *The solid lines show results of modeling. Sticking coefficients* $\eta_{12} = 50\,\eta_{11}$ *and* $\eta_{13} = \eta_{22} = \eta_{11}$.

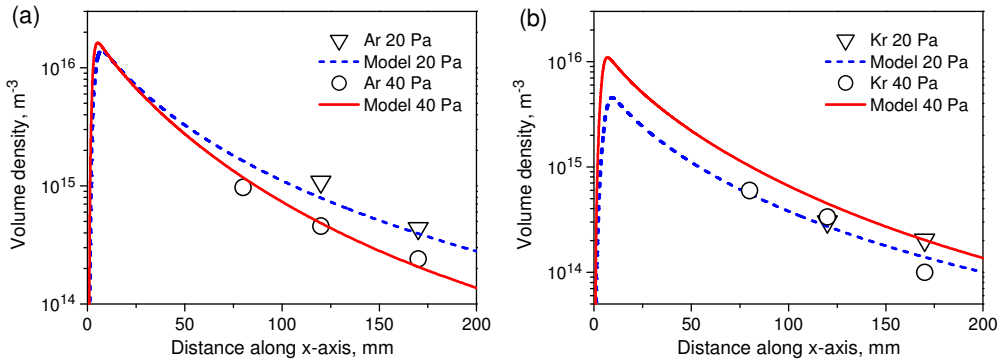

Figure 5.12. Dependence of volume density of Cu nanoparticles on the distance from the Cu target in the aggregation tube filled with argon (a) and krypton (b). Experimental data are shown by symbols.

5.4 Conclusions

The following conclusions can be drawn:

1. Several basic tests were performed with the experimental setup to explore its capabilities. The influence of different parameters on the formation of nanoclusters was investigated. Using these results further experiments were focused on processes in the aggregation chamber.
2. The formation of Cu nanoclusters in NC200-UHV nanocluster source inside of the aggregation chamber was studied. Experiments were performed with two types of gas, Ar and Kr, and at two different pressures, 20 and 40 Pa. As revealed by TEM, near the exit of the aggregation chamber the nanoclusters are fractal-like.
3. The experimental data were used to validate the model of cluster formation and coagulation in the inert gas which has been formulated in Chapter 4. For properly chosen parameters a good agreement has been obtained between the experimental data and predictions of the model. This means that the model can be used as a practical tool in planning future experiments with nanoparticles production in NC200-UHV nanocluster source and similar installations. For example, in the model the nanoparticles size distribution can be manipulated by selecting the type of target, the sputtering yield of precursor (that is controlled by the power supplied to the magnetron), the exit aperture size, the type and flow rate of inert gas, temperature in the aggregation tube, etc.

5.5 References

1. Moriarty P., Rep. Prog. Phys. 64 (2001) 297.
2. Liu J. P., Gutfleisch O., Fullerton E. and Sellmyer D. (eds.) *Nanoscale magnetic materials and applications,* New York, Springer, 2009.
3. Claridge S. A., Castleman A. W. Jr, Khanna S. N., Murray C. B., Sen A. and Weiss P. S., ACS Nano, 3(2) (2009) 244.
4. Haberland H., Karrais M., Mall M. and Thurner Y., J. Vac. Sci. Technol. A10 (1992) 3266.
5. Palmer R. E., Pratontep S. and Boyen H.-G., Nature Mater. 2 (2003) 443.
6. Turkin A. A., Dutka M. V., Pei Y. T., Vainshtein D. I. and De Hosson J. Th. M., J. Appl. Phys. 111 (2012) 124326.
7. Koch S. A., *Functionality and dynamics of deposited metal nanoclusters*, Thesis, University of Groningen, 2005.
8. Wasa K., Kitabatake M. and Adachi H. *Thin film materials technology sputtering of compound materials,* Heidelberg, Springer-Verlag, 2012.
9. Smirnov B. M., Dutka M., van Essen V. M., Gersen S., Visser P., Vainchtein D., De Hosson J. Th. M., Levinsky H. B. and Mokhov A. V., Europhys. Lett. 98 (2012) 66005.
10. Boldridge D., J. Aerosol Sci. 44 (2010) 182.

11. Soille P., *Morphological Image Analysis: Principles and Applications,* New York, Springer-Verlag, 2003.
12. Brasil A. M., Farias T. L. and Carvalho M. G., J. Aerosol Sci. 30 (1999) 1379.
13. Friedlander S. K. *Smoke, Dust and Haze: Fundamentals of Aerosol Dynamics,* 2nd edn. Oxford University Press, 2000.
14. Sorensen C. M., Aerosol Sci. and Technology 45 (2011) 765.